Advanced Net Flux Radiometer for the Ice Giants

S. Aslam[1,*], R. K. Achterberg[2], S. B. Calcutt[3], V. Cottini[2], N. J. P. Gorius[4], T. Hewagama[2], P. G. Irwin[3], C. A. Nixon[1], G. Quilligan[1], M. C. Roos[3], A. A. Simon[1], D. Tran[4], and G. Villanueva[1]

[1]*NASA Goddard Space Flight Center, Greenbelt, MD 20771, U.S.A*
[2]*University of Maryland, College Park, MD 20742, U.S.A.*
[3]*Oxford University, Parks Rd., OX1 3PU, U.K.*
[4]*Catholic University of America, Washington, DC 20064, U.S.A.*

([*]E-mail: shahid.aslam-1@nasa.gov)

Abstract: The design of an advanced Net Flux Radiometer (NFR), for inclusion as a payload on a future Ice Giants Probe mission, is given. The Ice Giants NFR (IG-NFR) will measure the upward and downward radiation flux (hence net radiation flux), in seven spectral bands, spanning the range from solar to far infra-red wavelengths, each with a 5° Field-Of-View (FOV) and in five sequential view angles (±80°, ±45°, and 0°) as a function of altitude. IG-NFR measurements within either Uranus or Neptune's atmospheres, using dedicated spectral filter bands will help derive radiative heating and cooling profiles, and will significantly contribute to our understanding of the planet's atmospheric heat balance and structure, tropospheric 3-D flow, and compositions and opacities of the cloud layers. The IG-NFR uses an array of non-imaging Winston cones integrated to a matched thermopile detector Focal Plane Assembly (FPA), with individual bandpass filters, housed in a diamond windowed vacuum micro-vessel. The FPA thermopile detector signals are read out in parallel mode, amplified and processed by a multi-channel digitizer application specific integrated circuit (MCD ASIC) under field programmable gate array (FPGA) control. The vacuum micro-vessel rotates providing chopping between FOV's of upward and downward radiation fluxes. This unique design allows for small net flux measurements in the presence of large ambient fluxes and rapidly changing ambient temperatures during the Probe descent to ≥10 bar pressure.

Keywords: Net Flux Radiometer, Ice Giants, Neptune, Uranus, Atmospheric Heat Balance.

1. Introduction

The Ice Giants, Uranus and Neptune, are of significant scientific importance and the Ice Giants Pre-Decadal Survey Mission Study Report (IGPDS, 2017) has identified the high priority of an exploration mission with an orbiter and a probe to one of the ice giants with preferential launch dates in the 2029-2034 timeframe. Such a mission will advance our understanding of the Solar System, exoplanetary systems, planetary formation and evolution. Twelve science objectives were identified by the IGPDS report and the Vision and Voyages Planetary Science Decadal Survey for ice giant exploration; hereafter referred to as V&V (NRC, 2011). Two main questions of equal scientific importance that relate to the atmospheric (thermal) structure of these icy worlds arise: (i) what is the planet's atmospheric heat balance? and (ii) what determines the planet's tropospheric 3-D flow? The IG-NFR concept, Fig. 1, onboard a probe descending deep into the atmosphere will contribute greatly to answering these questions by measuring the upward and downward radiation flux, in seven spectral channels, each with a 5° Field-Of-View (FOV) and in five sequential view (sky) angles as a function of altitude/pressure. For both Uranus and Neptune, 5° FOV observations at one scale height above the 1 bar level captures the radiation field from 1 bar to ~7 mb, a region of solar heating and predicted location of the CH_4 ice cloud.

The IG-NFR is designed to exceed baseline instrument requirements discussed in the IGPDS study Science Traceability Matrix (STM). The IGPDS study baselines the Galileo probe NFR (Sromovsky *et al.*, 1992, 1998). The science objectives and the features for both instruments are given in Table 1. The IG-NFR will have more capability with extra viewing angles and narrower FOV's to look for hemispheric dichotomies. The IG-NFR achieves all the science goals, with the necessary signal-to-noise ratio (SNR) in filter bands spanning the spectral range 0.2 to 300 µm. At the lowest anticipated temperature, for example 50 K at Neptune at a pressure of 0.1 bar, the long-wavelength cut-off at 300 µm, in the bandpass filter set, amply captures the tail of the Planck function which peaks at ~58 µm. Additionally, the IG-NFR will serve to provide an *in situ* reference for the remote sensing from visible-wavelength cameras and VIS-NIR mapping spectrometers' radiative transfer analysis of cloud structure, removing significant ambiguity that necessarily remains in the remote sensing retrievals.

The IG-NFR FPA is comprised of integrated detector and Winston cone subassemblies, housed inside a vacuum micro-vessel, Fig. 1. The vacuum micro-vessel helps mitigate the effects of rapid changes in temperature of the FPA that the instrument will experience during a Probe descent into either a Uranus or a Neptune atmosphere.

The nominal measurement regime for the IG-NFR extends from about 0.1 bar to at least 10 bars. In the following we first briefly describe the scientific objectives, then describe the IG-NFR instrument design and how it functions with particular emphasis on the FPA housed in the vacuum micro-vessel, give an account of the front end-electronic readout, give a radiometric calibration scheme and finally give the expected radiometric performance.

2. Scientific Objectives

Ice giant meteorology regimes depend on internal heat flux levels. Both incident solar insolation and thermal energy from the planetary interior, can have altitude and location dependent variations. Such radiative energy differences cause atmospheric heating and cooling, and result in buoyancy differences that are the primary driving force for Uranus and Neptune's atmospheric motions (Allison *et al.*, 1991; Bishop *et al.*, 1995). The three-dimensional, planetary-scale circulation pattern, as well as smaller-scale storms and convection, are the primary mechanisms for energy and mass transport in the ice giant atmospheres, and are important for understanding planetary structure, circulation, and evolution (Lissauer, 2005; Dodson-Robinson *et al.*, 2010; Turrini *et al.*, 2014). These processes couple different vertical regions of the atmosphere, and must be understood to infer properties of the deeper atmosphere and cloud decks (Fig. 2).

The atmospheres of Uranus and Neptune are expected to resemble Jupiter and Saturn's in the broad sense, with convective tropospheres giving way to radiatively regulated stratospheres at pressure levels of around 0.1 bar (~50-100 km altitude above the cloud tops). However, there are likely to be many differences in detail due to variations in composition and distance from the Sun, Table 2. The solar constant drops from ~51 W/m^2 at Jupiter to 15 W/m^2 at Saturn, 3.7 W/m^2 at Uranus, and 1.5 W/m^2 at Neptune, leading to progressively colder atmospheric temperatures. While on Jupiter and Saturn ammonia, ammonium hydrosulfide (NH_4SH) and water are predicted to be key cloud-forming species in the troposphere, the colder atmospheres of Uranus and Neptune are expected to form clouds from methane ice and hydrogen sulfide ice at observable pressure levels. Many authors have given thermochemical models and predictions of the main cloud layers as a function of compound abundances (*e.g.,* Baines *et al.*, 1994; Baines *et al.*, 1995; Atreya *et al.*, 2004; Irwin 2009; Irwin *et al.*, 2014; Mousis *et al.*, 2018). Observations at microwave wavelengths with the VLA found a missing component of continuum absorption (de Pater *et al.*, 1985, 1989, 1991) that was concluded to most likely arise from the pressure-broadened wings of H_2S lines and recent observations at near-infrared wavelengths (Irwin *et al.*, 2018, 2019) have directly detected absorption lines of H_2S above the main observable cloud deck on Uranus and Neptune. Hence, it now appears that the abundance of H_2S exceeds that of NH_3 in the observable atmosphere of Uranus and Neptune, which react/condense together to form a cloud of NH_4SH at a pressure of ~40 bars, leaving the left-over H_2S to condense alone at 3-5 bar. Figure 3(a) shows the distribution of NH_3 and H_2S absorption lines as a function of wavelength. Fig. 3(b) and Fig. 3(c) show the results of a first order, cloud structure of Neptune and Uranus calculated using an Equilibrium Cloud Condensation Model (ECCM) that employs basic principles of thermodynamics (Irwin, 2009). The cloud densities represent upper limits, as cloud microphysical processes (precipitation) would almost certainly reduce the density by factors of $10^2/10^3$ or more.

It is not known in detail how the energy inputs to the atmosphere–solar insolation from above and the remnant heat-of-formation from below interact to create the planetary-scale patterns seen on these ice giants (IGPDS, 2017). An understanding of circulation in these planetary systems requires knowledge of the vertical profile of radiative heating and cooling and also its horizontal distribution. *In situ* measurements with the IG-NFR, using judiciously chosen filter channels, will contribute to our understanding of the balance between the upward and downward radiation flux's to evaluate effects due to primary opacity sources, and to establish the extent of solar heating *e.g.*, below 1 bar pressure for the ice giants.

Given the ice giants' importance to our understanding of the formation of our solar system and the processes that have shaped it, as well as how common they are in exoplanetary systems, the V&V made these poorly studied worlds a priority. An ice giant mission was identified as among the top 3 Flagship-class missions. The Science Definition Team (SDT) of the IGPDS reaffirmed the importance of a

Flagship mission to an ice giant and the science goals and objectives that were defined by the SDT in their STM were consistent with those in V&V.

Twelve science objectives were identified in the STM of which two are highly relevant to the IG-NFR. The two science objectives to (i) determine the planet's atmospheric heat balance and (ii) determine the planet's tropospheric 3-D flow are intricately linked. It is not known how the energy inputs to the atmosphere are distributed and how these inputs interact to create the planetary-scale patterns. Important questions arise: What are the altitudes/pressures and compositions of the cloud layers? How do the cloud layers interact with solar visible and planetary thermal radiation to influence the atmospheric energy balance? How does the energy balance contribute to atmospheric dynamics? Is the intrinsic flux spatially inhomogeneous? Is there a hemispheric dichotomy? Can the intrinsic flux of Uranus or Neptune be detected? What is the nature of convection and circulation on the planets and how does it couple to the temperature field? To answer these questions a IG-NFR will provide unique *in situ* measurements, as the probe descends deep into the atmosphere, of solar insolation and thermal emission in five viewing angles with narrow fields of view and will provide complementary data to science instruments measuring visible albedo and thermal emission at a range of solar phase angles and incidence angles from an orbiter. Currently, three baseline spectral channels have been identified, listed in Table 3, that include a broadband solar channel (0.2-3.5 μm) for total deposition of solar radiation and hot spot detection, a broadband thermal channel (2.5-300 μm) for deposition/loss of thermal radiation and a broadband channel (0.6-3.5 μm) for solar deposition in the methane absorption region and cloud particles. The remaining four science spectral channels will be optimized using radiative transfer modelling studies, using NEMISIS (Irwin *et al.*, 2008) and the Planetary Spectrum Generator (Villaneuva *et al.*, 2017) codes, that are currently underway. Results of this modelling will identify optimal spectral channels for sensitivity and discrimination between cloud and H_2S, NH_3, H_2O and CH_4 gaseous abundances, and will be reported in a future publication.

2.1 *In situ* Net Energy Flux Measurement

The net energy flux, the difference between upward and downward radiative energy crossing a horizontal surface per unit area is directly related to the radiative heating or cooling of the local atmosphere: the radiative power per unit area absorbed by an infinitesimal thin atmospheric layer is equal to the difference in net fluxes at the boundaries of the layer. At any point in the atmosphere, radiative power absorbed per unit volume is thus given by the vertical derivative of net flux (dF/dz) in the plane-parallel approximation where the flux is horizontally uniform; the corresponding heating rate is then $(dF/dz)/(\rho C_p)$, where ρ is the local atmospheric density and C_p is the local atmospheric specific heat at constant pressure.

For the ice giants, the thermal structure and the nominal IG-NFR measurement regime extends from ~0.1 bar (near the tropopause which coincides with the temperature minimum) to 10 bar (ideally ≥50 bar). The 1986 Voyager encounter at Uranus (in the vicinity of the summer solstice) revealed very little details on atmospheric phenomena. However, distinctive bright high-altitude CH_4 ice clouds have been observed more and more frequently moving toward the northern spring equinox in 2008 and in subsequent years (de Pater *et al.*, 2015). During this Voyager encounter Neptune displayed an ice cloud layer at ~1 bar. More recent observations show these CH_4 clouds to be transitory and patchy in the 400 mbar to 1 bar level believed to be associated with convective upwelling (Karkoschka *et al.*, 2011; Irwin *et al.*, 2019). Atreya *et al.*, (2004) predicted the base of the water-ice cloud for solar composition O/H to be at ~40 bar level, and the NH_3H_2O solution clouds ~80 bar. However, the ice giants are likely to be significantly enriched in heavy elements compared to the Sun. This pushes the water cloud down to much higher pressures. Using the heavy-element enrichment suggested by a number of authors it is expected that NH_4SH clouds are at ~30 bar, HS clouds at ~4-5 bar and CH_4 clouds at <1.5 bar pressure (Irwin, 2009). So far, for Uranus, only an upper limit is known for its heat flow based on Voyager 2 (Pearl *et al.*, 1990). *In situ* probe measurements will help to define sources and sinks of planetary radiation, regions of solar energy deposition, and provide constraints on atmospheric composition and cloud layers.

2.2 State-of-the-art

Jupiter's Galileo probe made its first measurements on December 7th, 1995 (Sromovsky *et al.*, 1998). Cassini's Huygens probe included the Descent Imager/Spectral Radiometer (DISR) (Tomasko *et al.*, 2002) and landed on Titan on January 14th, 2005. DISR only looked at upward and downward direct and diffuse solar flux between 0.35 and 1.7 μm spectral range during its descent. To our knowledge, since the days of the Galileo probe no net flux radiometer, that included solar and thermal channels, has been on-board an atmospheric entry probe. Table 4 compares the Galileo probe NFR with the IG-NFR.

3. Instrument Description

Since the days of the Galileo probe NFR, there have been substantial advancements in synthetic diamond windows, filters (interference and mesh), uncooled detectors, insulating materials, and radiation hard FPGA’s and ASIC electronic readout technologies, which allows for a more capable and robust NFR. In order to meet the science objectives, the NFR was designed to have (i) seven spectral channels; (ii) a clear unobstructed 5° FOV for each spectral channel; (iv) thermopile detectors that can measure a change of flux of at least 0.5 W/m2 per decade of pressure; (iii) five distinct view angles (±80°, ±45°, and 0°); (iv) a detector response that can be predicted with changing temperature environment; (v) an FPGA controlled MCD ASIC technology for detector readout; (vi) signal processing that can integrate radiance for 1s or longer, and (vii) sampling that can view each angle including calibration targets every 10 s (assuming 100 m/ s descent rate).

The NFR concept (Aslam *et al.*, 2015, 2018, 2019; Mousis *et al.*, 2018) is shown in Fig. 4. Fig. 5 shows the Winston cone non-imaging optics, detectors, filters and fold mirror all housed in a vacuum micro-vessel so as to mitigate rapid excursions of temperature during the probe descent. A close hexagonal-packing array of Winston cones gives seven channels, with each Winston cone designed to give a 5° clear FOV. The Winston cone design can easily be changed to accommodate a larger FOV, resulting in a larger detector signal and a more compact vacuum micro-vessel design, since the Winston cone lengths will be smaller. Uncooled single pixel thermopile detectors are chosen for good detection sensitivity of radiation flux. A stepper motor with the aid of a gearbox rotates the vacuum micro-vessel, to each of the five view angles, so that the diamond window on the micro-vessel has an unobstructed view through apertures in the outer housing into the atmosphere. The outer housing (not shown in Fig. 5 for clarity) accommodates hot and cold targets and a light emitting diode for radiometric calibration for each sequence of measurements (5-views). The technical specifications of the NFR are given in Table 5.

The system block diagram is shown in Fig. 6 and highlights the major subsystems in the FPA, comprising the thermopile detector sub-assembly and the Winston cone sub-assembly. The FPA is integrated to the fold mirror sub-assembly and aligned and assembled into a vacuum micro-vessel as shown in Fig. 5. The FPA detector and thermistor signals are read out via an MDM connector to the Front End Electronics (FEE) *i.e.,* a MCD ASIC that communicates to a FPGA.

3.1 Focal Plane Assembly

The FPA consists of a Winston cone sub-assembly integrated to a detector sub-assembly. The Winston cone sub-assembly is shown in Fig. 5 with specifications shown in Fig. 7. The center-to-center distance of entrance diameters of two cones is 10 mm. The detector sub-assembly is also shown in Fig. 5. The detector fanout board is shown in Fig. 8, which accommodates seven thermopile detectors packaged in TO-39 housings manufactured by Micro-Hybrid Electronic GmbH, Germany. One dark reference detector is mounted on the backside of the fanout board. Thermistors mounted in the TO-39 housings and on the fanout board allow for precise temperature measurement of the detectors and the environment ensuring thermal compensation corrections can be applied to the measurements. Terminal pins on the fanout board are connected to the MCD ASIC readout circuit by a shielded cable to reduce interference noise (not shown). Thermopile detector parameters are listed in Table 6. For the IG-NFR, eight thermopile pixels (7 science + 1 blind) and 9 thermistor signal outputs will be captured simultaneously by the MCD ASIC and processed in parallel under FPGA control. The DAC integrated on the MCD is used to generate a pixel reference to position the output signals of the thermopiles.

3.2 MCD ASIC Readout

The MCD ASIC (5 mm x 5 mm chip) is a fully custom radiation-hardened-by-design (RHBD) integrated circuit that was designed using Towerjazz Semiconductor's 180 nm CMOS CA18HD process node for near-DC signal parallel readout, Fig. 9, (Quilligan *et al.*, 2014, 2015; Aslam *et al.*, 2012). The MCD ASIC has twenty readout channels each comprising a low noise variable gain amplifier driving a dedicated high-resolution sigma-delta A/D converter (ΣΔ ADC). The channels are designed to interface directly to thermopile outputs and amplify/digitize the signals with variable gain/resolution. Effective 20-bit digitization of the signals can be attained by using the analog front-end gain and oversampling ratio. The original design targeted a proposed Europa Clipper thermal instrument (Aslam *et al.*, 2016) readout for operation in the harsh Jovian orbital environment, *i.e.,* immunity to > 3 Mrad (Si) total ionizing dose (TID). The MCD ASIC also has a multiplexed buffered ΣΔ ADC for general purpose (housekeeping) tasks, 10 DACs, a serial port and a die temperature sensor. The Towerjazz process node CA18HD was selected because it has inherent radiation tolerance and immunity to latch-up. With the addition of RHBD techniques, the MCD was hardened to levels that far exceed the original design requirements.

3.2.1 *MCD ASIC Resolution*

The ΣΔ ADCs utilize oversampling to quantize their inputs. ΣΔ conversion is used because the thermopile signal bandwidths are very low and the architecture is inherently linear. The effective resolution of the MCD digitizers is increased by a scheme which is a function of the (1) the analog front end (AFE) gain (variable) and (2) the oversampling ratio (OSR, also variable). 20 bits of resolution is achieved by choosing an appropriate AFE gain and OSR. The main barrier to achieving 20-bit resolution is noise, particularly *1/f*, Johnson and noise pickup from the environment. The MCD channels employ frequency translation, correlated double sampling and auto-zero to reduce *1/f* noise before being digitized by the ΣΔ ADCs. Active filtering within each channel reduces the Johnson noise. The signal paths from thermopile to ADC are pseudo-differential which reduces common-mode noise (Quilligan *et al.,* 2017, 2018, 2018). Each ADC outputs its data as a single bit stream for off-chip decimation and filtering, allowing the user to change the OSR and thus the ADC resolution.

3.2.2 *MCD ASIC Noise*

The thermopile detector outputs are directly connected to on-chip instrumentation amplifiers so as to minimize signal loss due to the high output impedances of the thermopiles. Since the thermopiles output very low frequency signals, the *1/f* noise of the readout electronics can be significant and thus must be mitigated along with the thermal noise contribution. To reduce readout *1/f* noise, the output signal of each detector is modulated at 64 kHz, amplified and then demodulated back to the baseband frequency region. Since signal amplification happens at high frequency, the input referred *1/f* noise of the detected signal is dramatically reduced. Fig. 10 shows the input analog path of one typical channel. Moreover, the variable gain amplifier is reconfigurable to avoid saturation.

The ∑∆ ADCs on the MCD ASIC utilize oversampling and noise shaping to achieve high resolution. As a result, most of the quantization noise is shifted to the high frequency region which can easily be filtered out with a digital filter (Fig. 11).

3.2.3 *MCD ASIC Radiation Qualification*

All of the circuitry in the MCD uses RHBD techniques including (a) enclosed layout transistors (ELTs) and (b) double guard ring isolation. The ELTs harden the circuits against total ionizing dose (TID) while the isolation rings help prevent single event latch-up (SEL). The first generation MCD ASIC was tested for TID at GSFC's radiation effects facility up to 53 Mrad (Si) TID with no increase in the supply current and very small parametric shifts in gain and offset (see Figs. 12 and 13). The ASIC was also tested with heavy ions up to 174 MeV-cm^2/mg at Texas A&M University's without latching up. Fig. 14 is a plot of MCD supply current and transient effects over time with the heavy ion beam both off and on. Supply current for the entire chip increases slightly due to charge deposition from the beam but this is bled off once the beam is deactivated. Fig. 14 also shows a plot of single event transients (SETs) at a high LET value. In this plot the MCD is digitizing a mid-scale signal from one channel at a channel gain of 25. When the beam turns on, the charge transients cause the channel auto-zero circuit to vary its correction voltage to the amplifier. Due to the pipeline nature of the channels, any single event upsets would get flushed out or corrected by the periodic refresh of the channel settings.

3.2.4 *MCD ASIC – FPGA Control*

An FPGA controls the MCD ASIC through a SPI serial protocol. During run time, the MCD ASIC channels output up to twenty 1-bit data streams from the ∑∆ ADCs to the FPGA where they get decimated back to useful multi-bit words. In this case, multiple parallel Sinc3 filters with a decimation ratio of 1024 were implemented on the FPGA. Fig. 15 shows the block diagram of the data acquisition module. Fig. 16(a) shows the MCD ASIC under FPGA control configuration to establish readout noise and Fig. 16(b) shows a typical noise spectrum when the output data rate is at approximately 240 Hz with a modulating frequency of 64 kHz, the input was shorted to the pixel reference to avoid interference from any external noise source. A typical readout channel exhibits an average spot noise of ~27 nV/√Hz. For a signal frequency that is lower than the output data rate, a moving average algorithm can be used to further reduce thermal noise and random noise from the signal. Fig. 16(b) also shows a 60 Hz notch filter response (to reject line interference) which was achieved by careful selection of the ADC clock frequency and the moving average. To verify the operation of the parallel readout circuit an infra-red broadband source was pulsed at 0.5 Hz, collimated and focused onto a quad thermopile detector array with distinct filter bands, centered at wavelengths 2.7 µm, 4.26 µm, 3.95 µm and 6.58 µm (for demonstration purpose only). The parallel readout ADC codes for the four spectral channels are shown in Fig. 17.

4. Radiometric Calibration

The basic equation relating digital count output in a given channel to the external radiation flux is essentially (Sromovsky *et al.*, 1992):

$$C = Kf(T/T_0)(L_u - L_d) \tag{1}$$

where K is an absolute calibration constant, $f(T/T_0)$ is a relative response function describing the instrument response dependence on detector temperature, and where L_u, L_d are the hemispherical integrals of radiance, *i.e.*, the up- and down average radiances within the FPA FOV respectively and are given by:

$$L_u = \int_0^\infty s_\lambda d\lambda \int_0^{\pi/2} \sin(\theta)\, d\theta \int_0^{2\pi} d\phi a_u(\theta,\phi) L(\theta,\phi,\lambda) \tag{2}$$

$$L_d = \int_0^\infty s_\lambda d\lambda \int_{\pi/2}^{\pi} \sin(\theta)\, d\theta \int_0^{2\pi} d\phi a_d(\theta,\phi) L(\theta,\phi,\lambda) \tag{3}$$

where s_λ is the relative spectral response at wavelength λ; $a(\theta,\phi)$ relative angular response at θ (angle from vertical), ϕ (azimuth angle); $L(\theta,\phi,\lambda)$, spectral radiance at wavelength λ angles θ,ϕ, where s_λ and $a(\theta,\phi)$ are both normalized to have unit integrals. Because the thermopile detectors are hermitically sealed, no response to external pressure is expected. Because the Winston cones have fixed FOVs, no crosstalk between the detectors is expected.

Consider a flat radiation field, as an extended area blackbody, then $L(\theta,\phi,\lambda)$ is given by the Planck radiance function $B_\lambda(T)$ and eqns. (2) and (3) become:

$$L_u = \int_0^\infty s_\lambda B_\lambda(T_u) d\lambda \int_0^{\pi/2} \sin(\theta)\, d\theta \int_0^{2\pi} d\phi a_u(\theta,\phi) \tag{4}$$

$$L_d = \int_0^\infty s_\lambda B_\lambda(T_d) d\lambda \int_{\pi/2}^{\pi} \sin(\theta)\, d\theta \int_0^{2\pi} d\phi a_d(\theta, \phi) \tag{5}$$

Which reduces to the spectrally weighted average of the net Planck radiance. For a spectrally flat broadband channel, the average net radiation, L_n, is simply $L_n = (L_u - L_d)$.

During test and validation in a simulated thermal-vacuum environment, the instrument will measure (i) relative angular response for each detector using a blackbody source operating at 500 K; (ii) relative spectral response for each spectral band (using a quartz halogen lamp between 0.2 and 3 μm and 1000 K SiC globar for wavelength 3 μm to about 40 μm); (iii) relative crosstalk coefficients between neighboring channels (ensure that this is less than 0.2%); (iv) relative response versus temperature for each channel and (v) absolute responsivity measurements for each channel using a source that fills the FPA FOV. The testing will also provide sufficient measurements to ensure that FPA digital count output as a function of input radiation flux and FPA temperature can be calculated and predicted.

5. Expected Radiometric Performance

The calculated SNR's for three of the defined baseline filter channels on an IG-NFR are given in Table 7. The calculations are based on the Winston cone étendue of 1.54$\times 10^{-7}$ sr.m^2, optical efficiency of 0.5, bandpass spectral radiances for both solar and thermal contributions taking into account solar reflection losses from the top of the atmosphere (0.3), the scene (0.7), emissivity of the scene (0.5), emissivity of optics (0.5), emissivity of housing (0.7) and averaging $(1/2\tau)$ based on the time constant (τ) of the detector (36 ms) over a 1 s integration time. The system Noise Equivalent Power (NEP) is derived from the detector responsivity (295 V/W) and the square root of the sum of the squares of all noise sources, *i.e.*, 12 bit quantization noise (0.25 μV), noise voltage (18 nV), readout noise (50 nV), and Johnson noise (1.8 nV) giving a system NEP of 0.9 nW.

Acknowledgements

We thank NASA Goddard Space Flight Center for research and development funds, and the NASA ROSES PICASSO program (*NNH17ZDA001N-PICASSO*) for supporting the design and technology maturation of the IG-NFR. We also wish to thank Ms. Maxine Alexandre-Strong, a 2019 NASA summer intern for proof reading this manuscript.

Table 1. Science Goals and comparison of IGPDS baseline NFR [1] with the IG-NFR.

Science Goal	Measurement	IGPDS Baseline NFR	Ice Giants NFR
Determine the planet's atmospheric heat balance	Net energy flux between 0.1 bar and 10 bar	NFR based on the Galileo probe heritage: 0.3 to 500 µm in five spectral bands designed for Jupiters atmosphere; 2 views ±45°; FOV ±20°	0.2 to 300 µm in seven spectral bands (see Table 3); 5 views ±80°, ±45° and 0°; FOV ±2.5°
Measure the planet's tropospheric 3-D flow (zonal, meridional, vertical)			

Table 2. Mean temperature for the gas and ice giants at 1 bar, showing the thermal emission peak wavelengths.

Planet	T (K)	λ_{peak} (μm)
Jupiter	165	17
Saturn	134	22
Uranus	76	38
Neptune	72	40

Table 3. Three of the seven IG-NFR science spectral filter channels that have been identified.

Ch#	**Wavelength (µm)**	**Objectives**
1	2.5-300	Deposition/loss of thermal radiation
2	0.6-3.5	Solar deposition in methane absorption region; cloud particles
3	0.2-3.5	Total deposition of solar radiation and hot spot detection
4-7	Under radiative transfer modelling studies for H_2S, NH_3, H_2O and CH_4 gaseous abundances and cloud opacities	
8	Blind	Reference

Table 4. Galileo NFR parameters compared to the IG-NFR.

Parameter	Galileo NFR	IG-NFR
Venting	Yes	Yes
Clear FOV	40°	5°
View angles	±45°	±80°, ±45° and 0°
Detectors	Pyroelectrics	Thermopiles
Number of channels	5 + 1 dark	7 + 1 dark
Window	Natural diamond	Synthetic diamond
Spectral range	0.3-500 µm	0.2-300 µm
Mass	3.1 kg	2.4 kg
Volume	13x20x16 cm^3	11x31x14 cm^3
Power	Not found	5.2 W
Telemetry	Not found	124 bps

Table 5. IG-NFR technical specifications designed to meet the science objectives for net energy flux measurements in the atmospheres of Uranus or Neptune.

Parameter	IG-NFR
Spectral range	0.2 to 300 µm
Optics	Non-imaging Winston cones
Channels	7 science + 1 blind
Field-Of-View	5°
Viewing angles	±80°; ±45° and 0° relative to nadir/zenith
Detectors (uncooled)	7 thermopile pixels + 1 dark
Pixel size	0.5 mm diameter
Mass	~ 2.4 kg
Basic power	~ 5.2 W
Envelope	(11 × 31× 14) cm^3
Data volume (90 mins)	670 kbits
Operating modes	36 ms integration
Observation strategy	Sequential rotation into five sky view angles

Table 6. Detector specifications. The thermopile detectors with gold black absorbers have essentially a flat spectral response from 0.2 to 300 µm. The detectors survive >38 W/m^2 (*c.f.* 3.7 W/m^2 solar constant at Uranus) so inadvertent FOV pointing at the sun during the probe decent will pose no risk.

Detector Parameter	Value
Manufacturer	µ-Hybrid (Germany)
Detector type	Thermopile
Detector material	Bi-Sb thin film
Package type	TO-39
Design waveband	0.2-to-300 µm
Pixel count	7 (+1 dark)
Pixel size	0.5 mm
Responsivity	~295 V/W
Time Constant	36 ms (-3 dB cut-off)
Noise voltage	~18 nV/√Hz
NEP	0.06 nW/√Hz
Operating Environment	Vacuum or inert gas

Table 7. Calculated SNRs for three of the seven spectral channels currently identified. SNR for weaker channels can be optimized by averaging over a longer integration time.

Channel (μm)		SNR		
		50K	100K	300K
1	2.5-300	46	632	50819
2	0.6-3.5	140	140	168
3	0.2-3.5	226	226	254

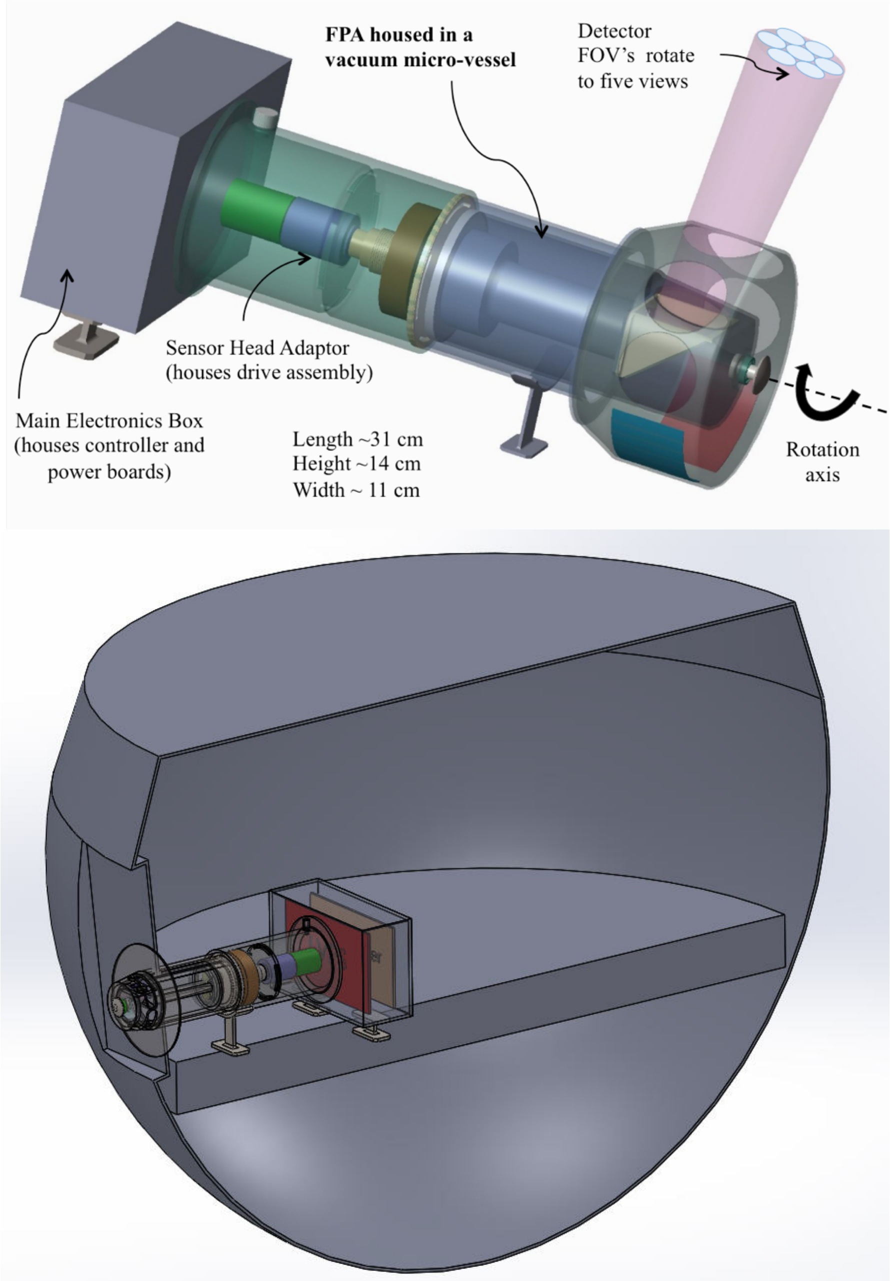

Figure 1. *Top:* IG-NFR concept responds to the science objectives of a future Ice Giants Probe mission to either Uranus or Neptune. The IG-NFR will be capable of measuring energy flux in seven spectral bands (channels) covering the 0.2-300 µm spectral range, each with a 5° FOV projected into the sky. *Bottom:* Graphic showing accommodation of the IG-NFR on a 1-m diameter probe deck.

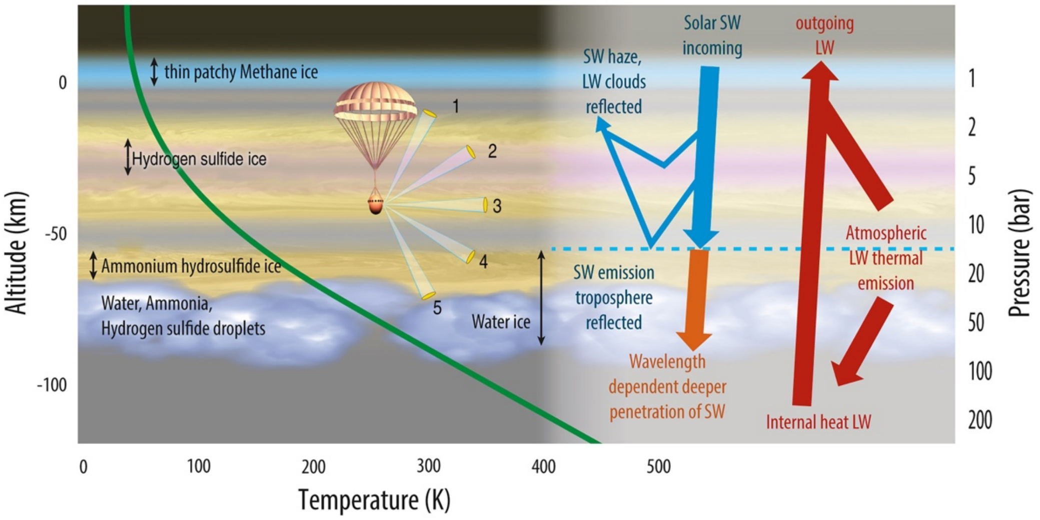

Figure 2. Cartoon of a Probe descent through either Uranus or Neptune's poorly understood atmospheres. The NFR will reveal thermal structure, opacity sources, and help provide a global radiative balance. As the probe descends, seven boresighted spectral channels measure energy flux, sequentially and repetitively (clockwise and anti-clockwise) at five viewing angles. The view angles in the cartoon (1-to-5) are shown at 1.5 s time intervals (1 s integration and 0.5 s slew to next position). The sequence repeats anti-clockwise (5-to-1). Each spectral channel samples different processes. Short Wave radiation - SW; Long Wave radiation - LW.

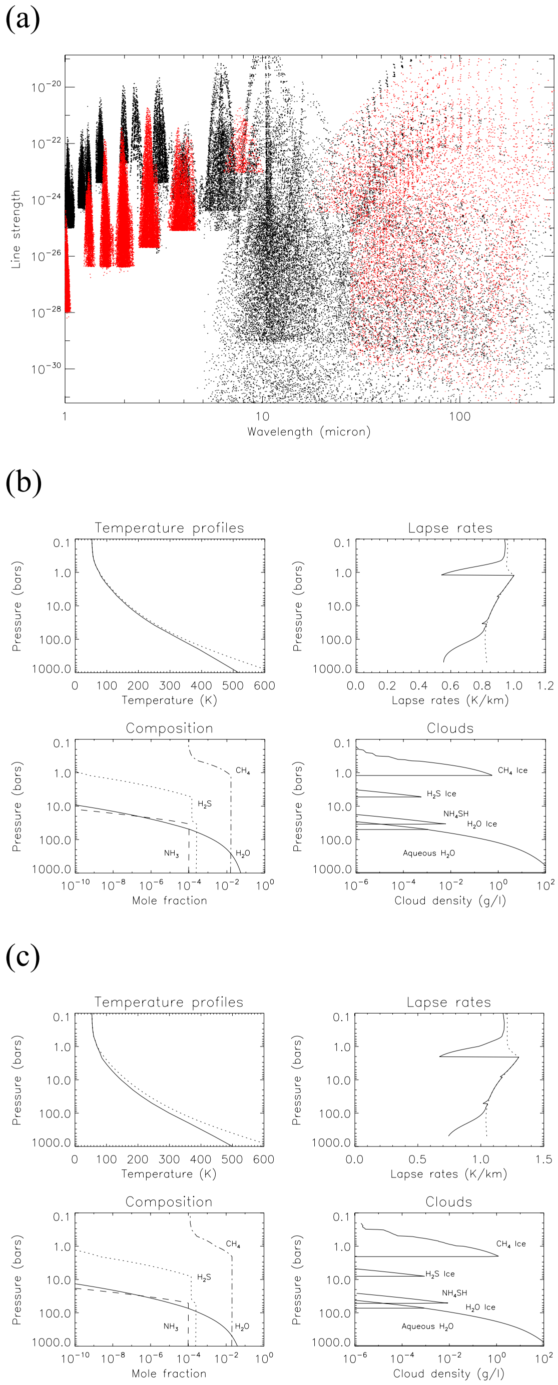

Figure 3. (a) Distribution of NH_3 (black) and H_2S (red) absorption lines as a function of wavelength (1-300 µm), courtesy of Irwin, private communication. (b) ECCM model of Uranus' atmosphere, calculated cloud layers: H_2O cloud (water, then ice) at $p > 1,000$ bar, NH_4SH at ~40 bar, H_2S ice at ~5 bar, and CH_4 ice at ~1.2 bar. Assumed composition: O/H = 100x the solar value, N/H = the solar value, S/H = 11x the solar value, C/H = 40x the solar value (Irwin, 1996). (c) ECCM model of Neptune's atmosphere, calculated cloud layers: H_2O cloud (water, then ice) at $p > 1,000$ bar, NH_4SH at ~50 bar, H_2S ice at ~8 bar, and CH_4 ice at ~2 bar. Assumed composition: O/H = 10x the solar value, N/H = the solar value, S/H = 11x the solar value, C/H = 50x the solar value (Irwin, 1996). An IG-NFR would provide crucial ground-truth measurements to test current models.

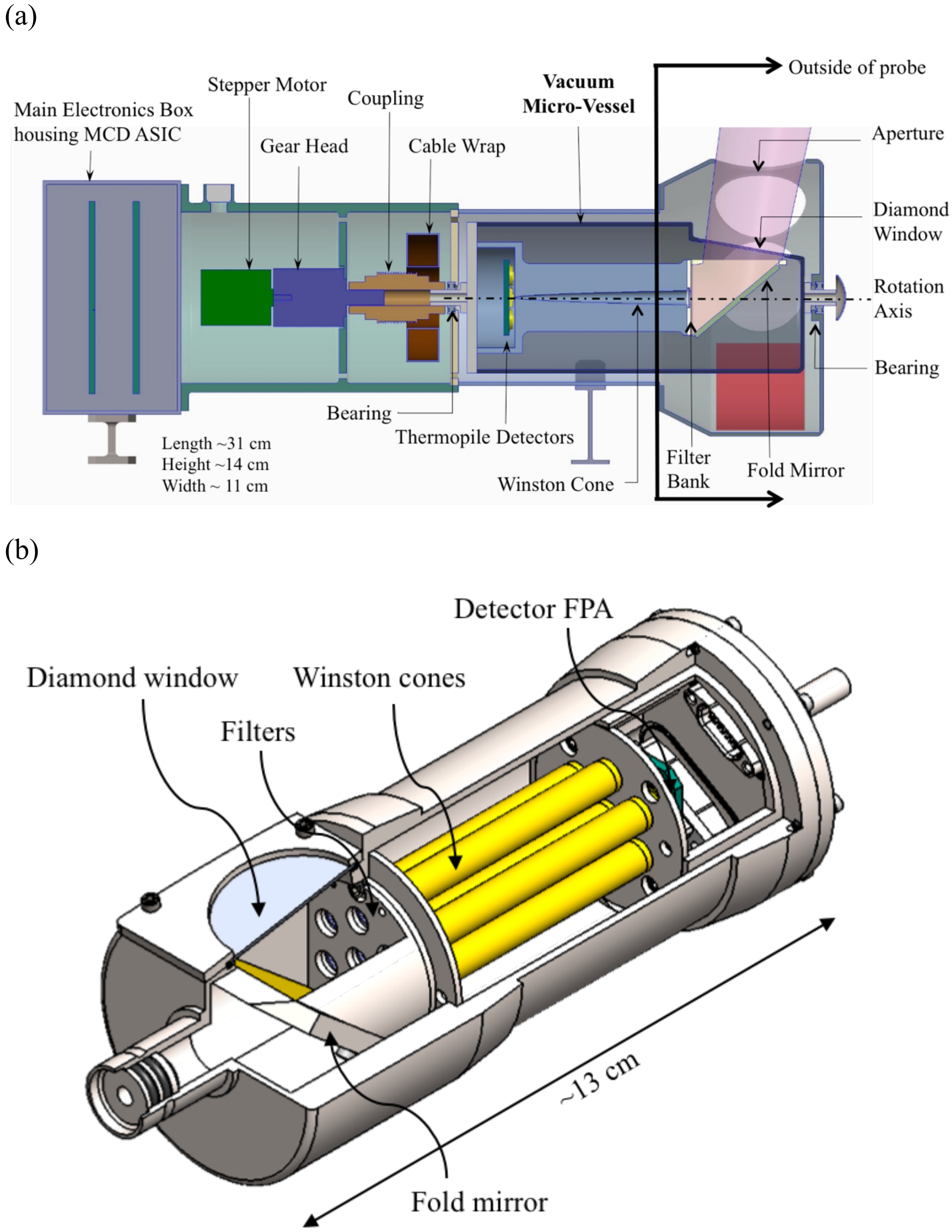

Figure 4. (a) Side view section of the IG-NFR concept. (b) Quarter view section of the vacuum micro-vessel with a diamond window, which houses the fold mirror, filters, Winston cones, and detector FPA, to minimize rapid temperature excursions during probe descent.

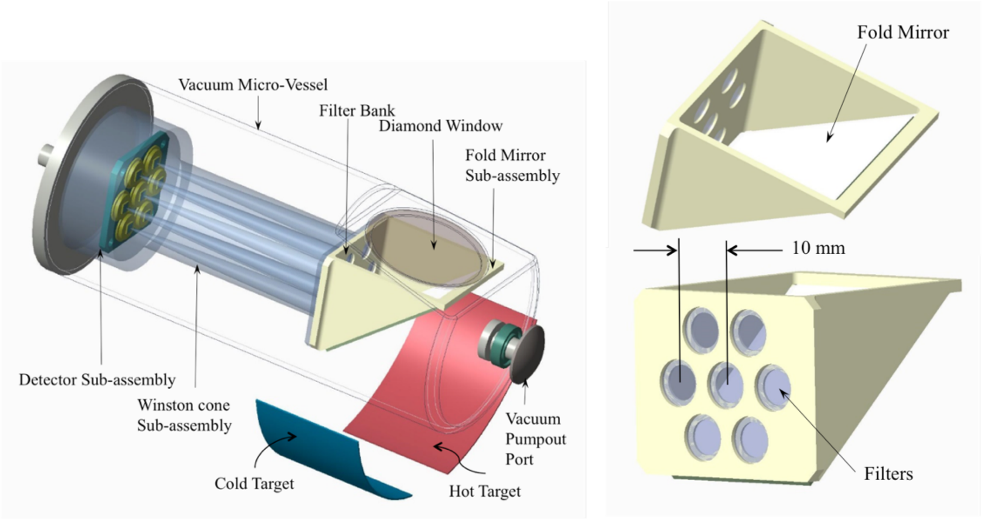

Figure 5. *Top*: Internals of the vacuum micro-vessel. *Bottom*: Fold mirror sub-assembly that includes the filter bank.

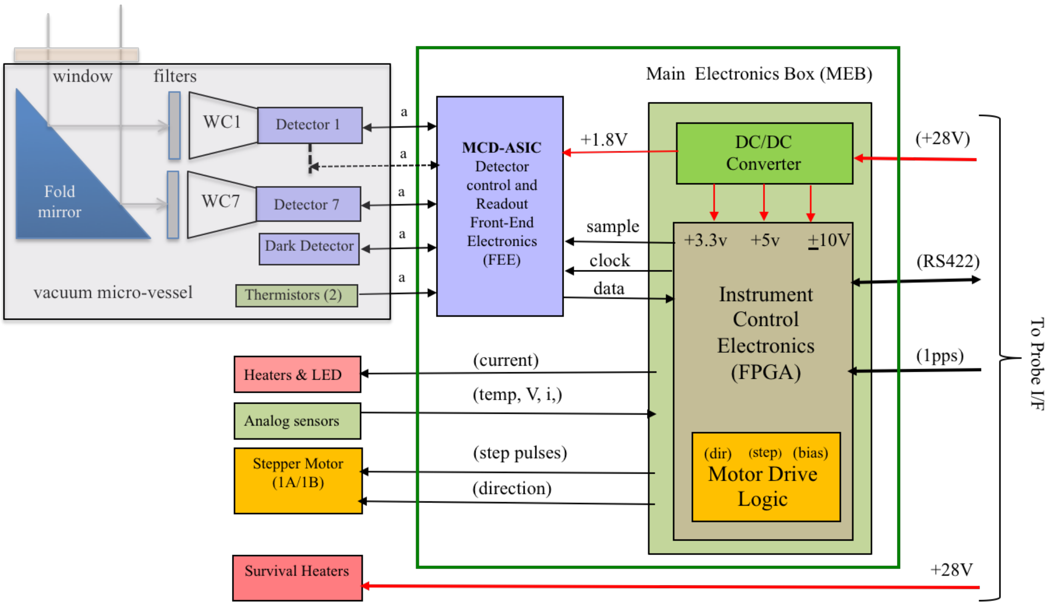

Figure 6. IG-NFR system block diagram. WC - Winston cone; a-analog.

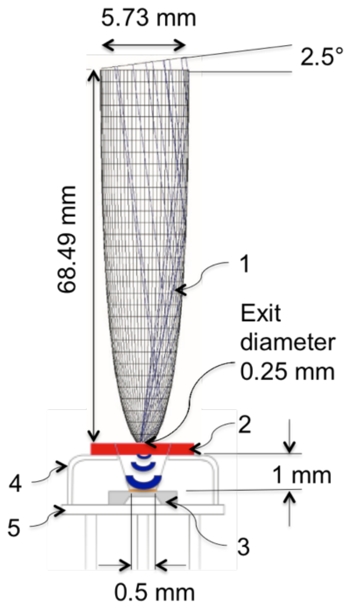

Figure 7. Geometry of Winston cone and thermopile detector. The output of the Winston cone touches the window. (1) Winston cone; (2) window; (3) thermopile chip; (4) cap; (5) header. Note: 2.5° defines half FOV (light rays perpindicular to the inclination are the only rays that are accepted into the Winston Cone).

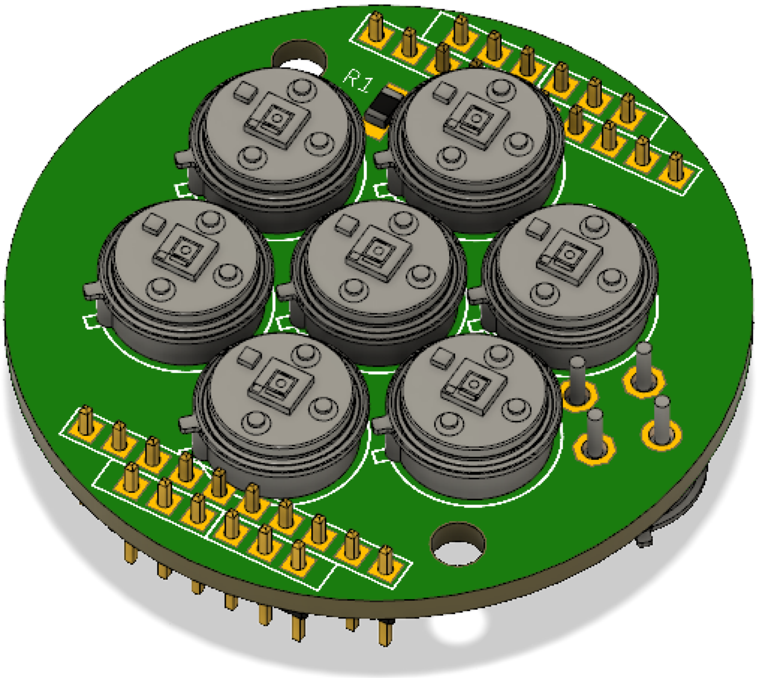

Figure 8. Thermopile detector fanout board with thermistor temperature readout. Each detector package also has a thermistor temperature sensor. Board dimension: ~ 4 cm diameter.

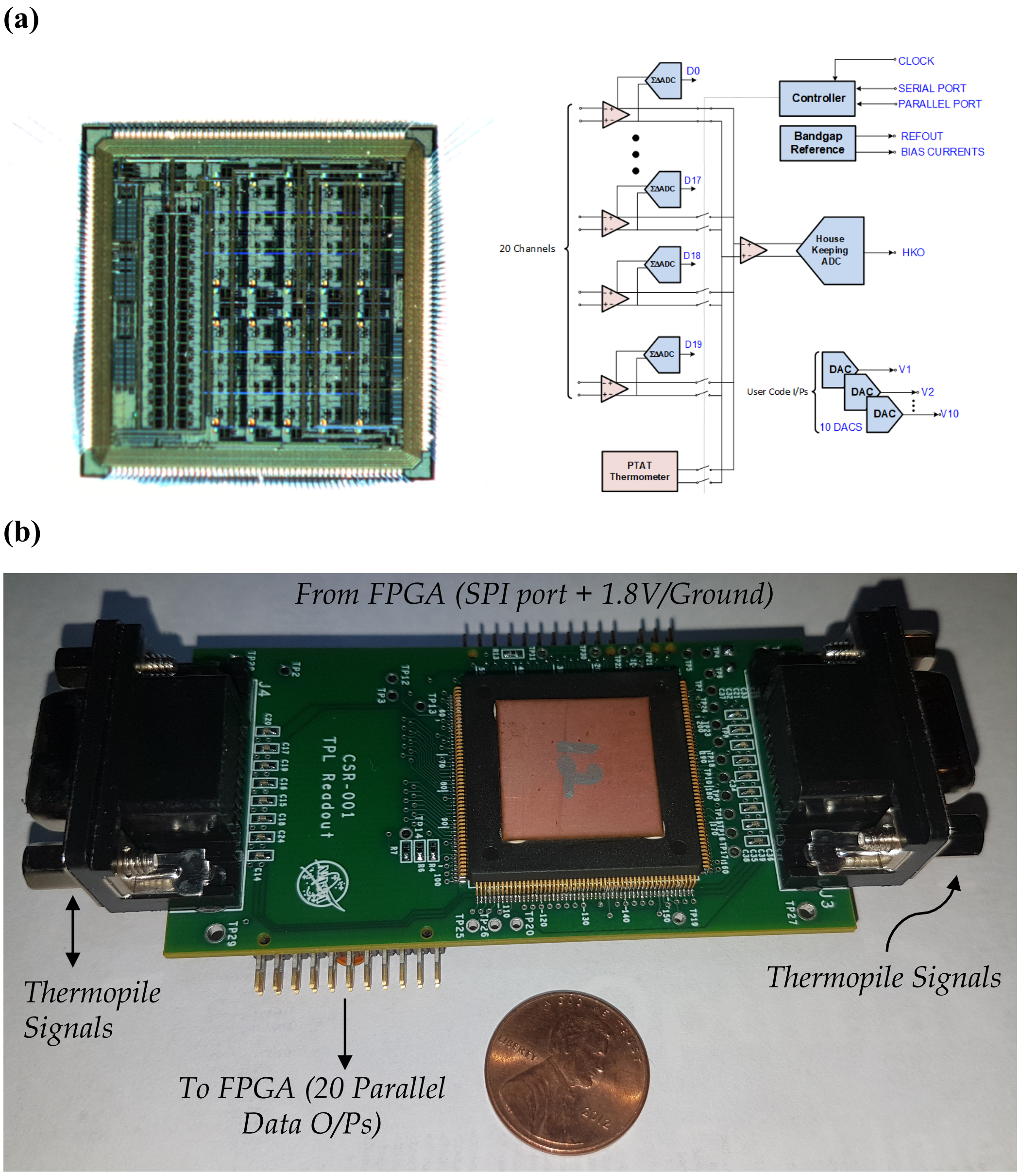

Figure 9. (a) MCD ASIC chip micrograph and simplified system block diagram; (b) 20-channel MCD ASIC board. This radiation hard MCD ASIC enables the IG-NFR thermopile readout electronics to be compact and to have small volume, mass and power.

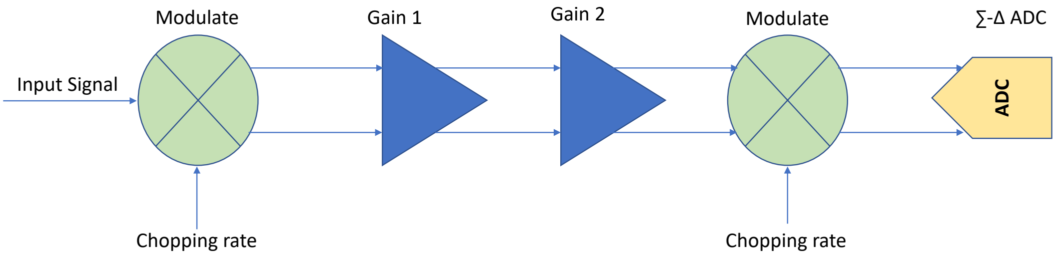

Figure 10. Analog input signal path of one typical MCD ASIC channel

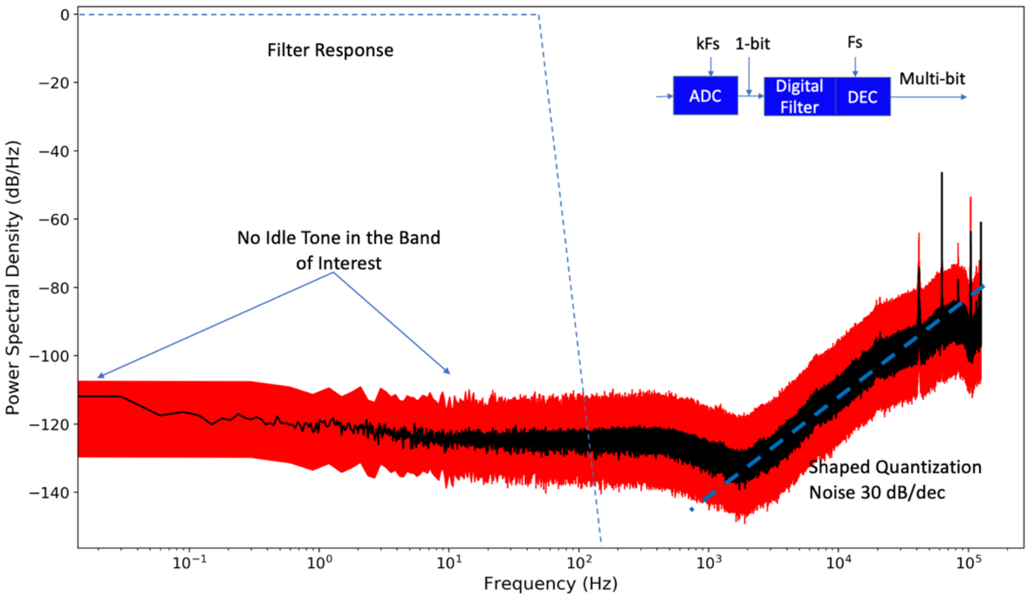

Figure 11. Measured noise spectral density of 1-bit stream from delta-sigma ADCs (average in black and ± 1 σ deviation in red from 20 measurements). Decimation filter on FPGA will remove high frequencies noise.

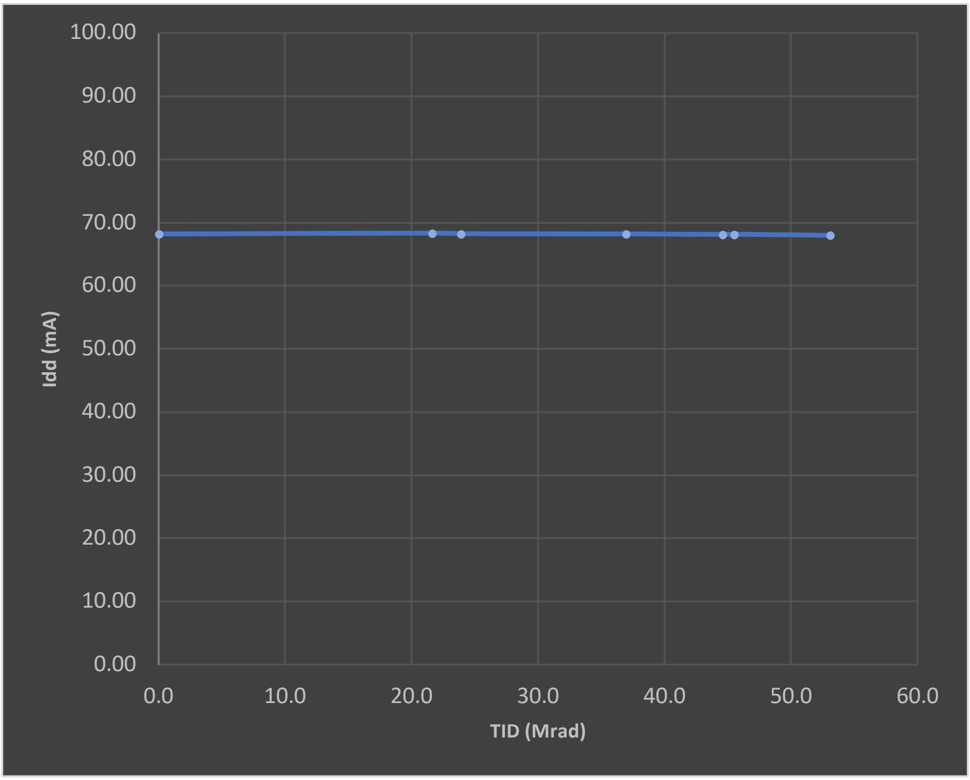

Figure 12. MCD ASIC supply current vs ionizing dose (dots indicate measurement points)

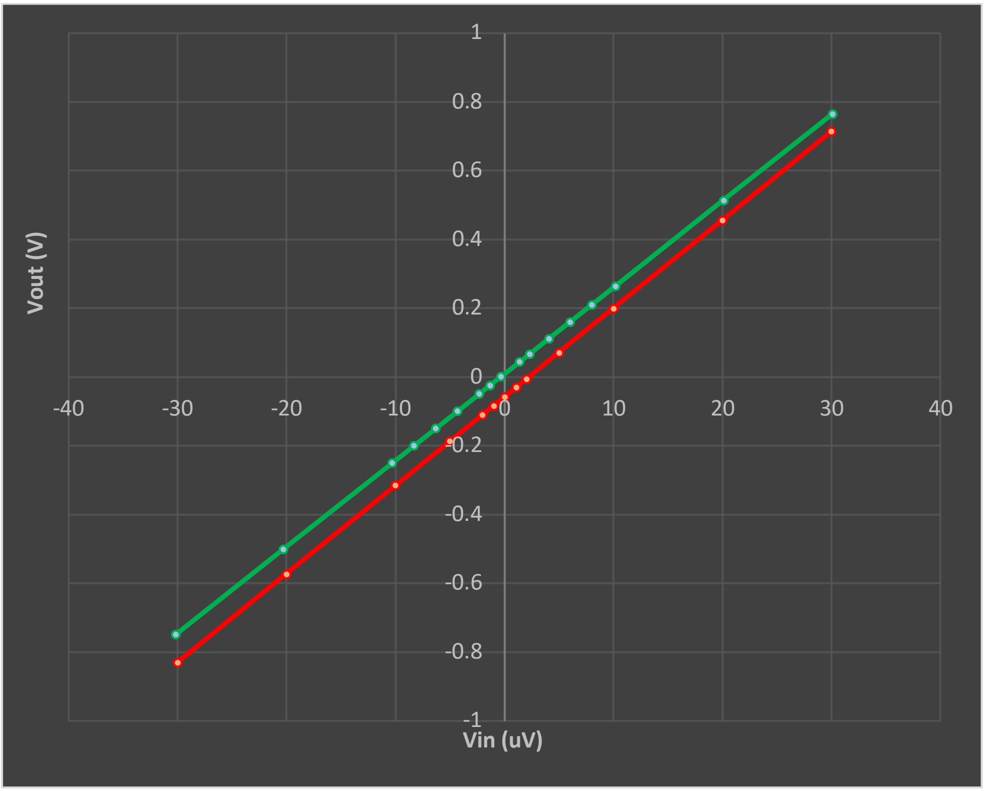

Figure 13. MCD ASIC transfer function for non-irradiated (green) vs post 50 Mrad (red) parts

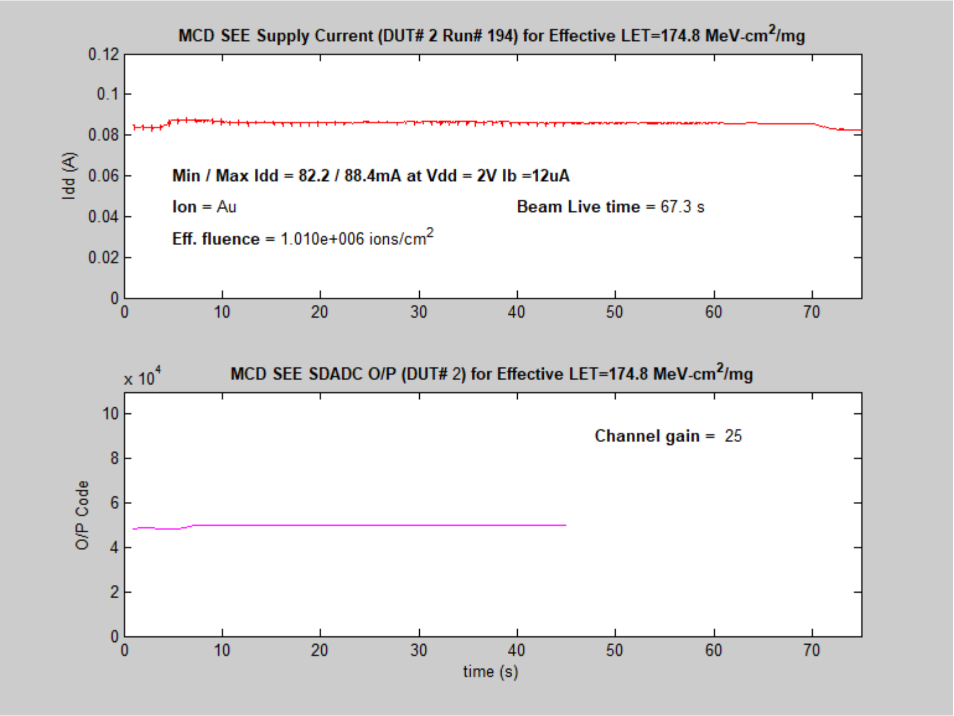

Figure 14. MCD ASIC supply current / SETs during heavy ion testing at TAMU at 174.8 MeV-cm^2/mg

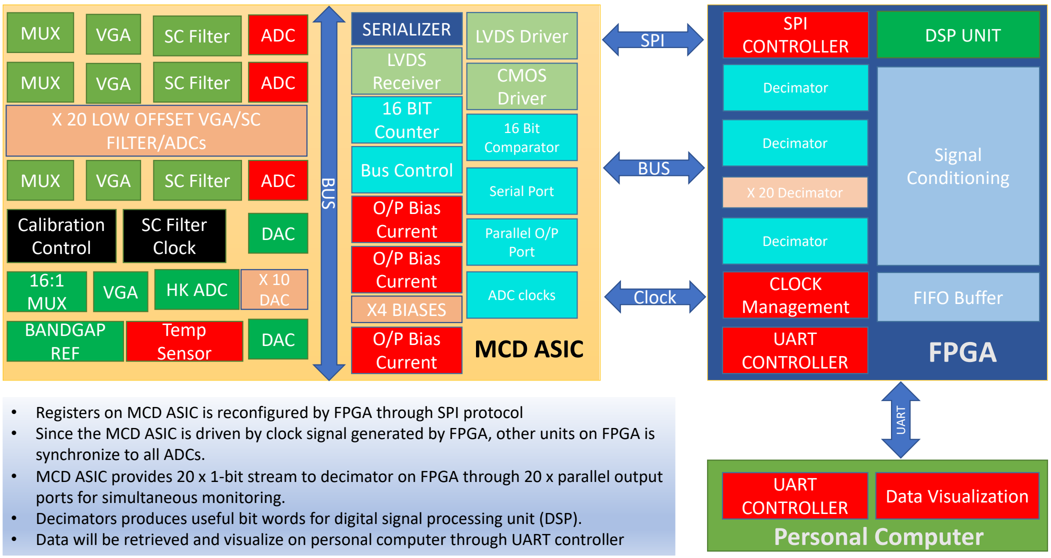

- Registers on MCD ASIC is reconfigured by FPGA through SPI protocol
- Since the MCD ASIC is driven by clock signal generated by FPGA, other units on FPGA is synchronize to all ADCs.
- MCD ASIC provides 20 x 1-bit stream to decimator on FPGA through 20 x parallel output ports for simultaneous monitoring.
- Decimators produces useful bit words for digital signal processing unit (DSP).
- Data will be retrieved and visualize on personal computer through UART controller

Figure 15. Block system diagram of the data acquisition system.

(a)

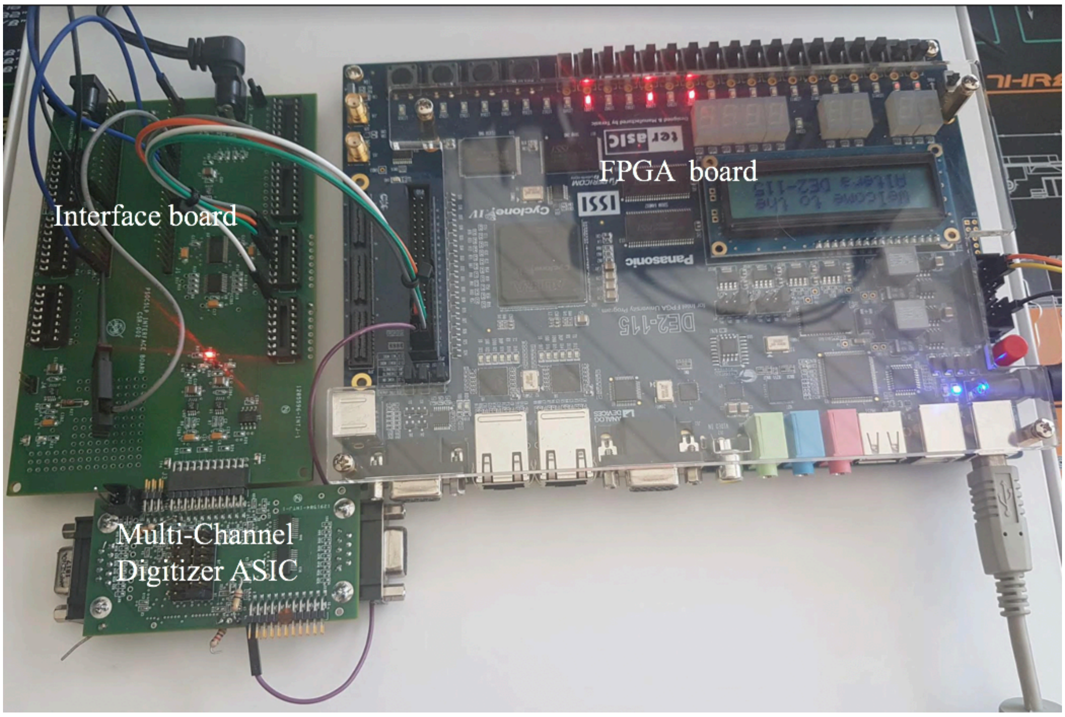

(b)

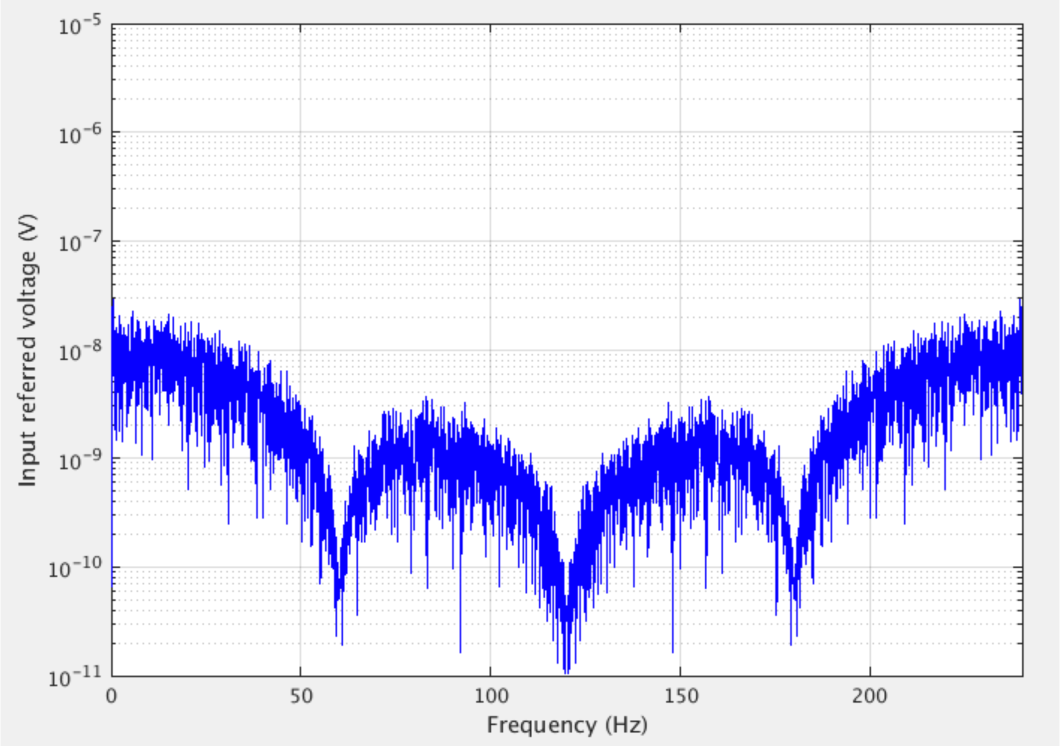

Figure 16. (a) Thermopile detector readout electronics; (b) Typical noise spectrum when the sampling rate is ~240 Hz with modulating frequency of 64 kHz, the input was shorted to the pixel reference to avoid interference from external noise source.

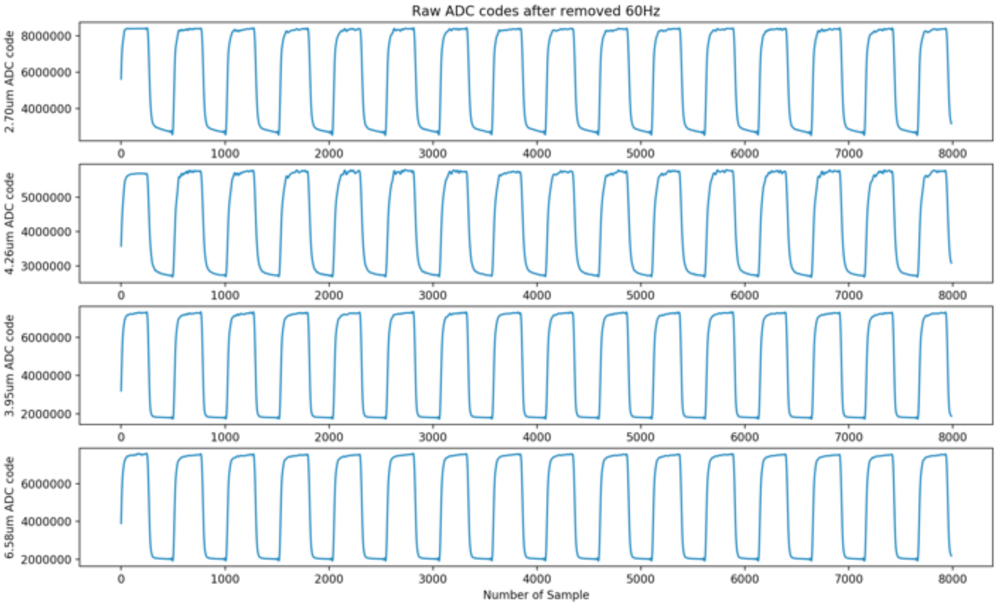

Figure 17. Parallel ADC code readout from a quad thermopile detector array with narrow band filters centered at wavelengths 2.7 µm, 4.26 µm, 3.95 µm and 6.58 µm.

References

Allison, M., Beebe, R. F., Conrath, B. J., Hinson, D. P., Ingersoll, A. P., 1991. Uranus atmospheric dynamics and circulation. Uranus p. 253-295.

Aslam, S., Akturk, A., Quilligan, G., 2012. A Radiation Hard Multi-Channel Digitizer ASIC for Operation in the Harsh Jovian Environment, In Extreme Environment Electronics, Ed. J. D. Cressler, H. A. Mantooth, CRC Press, Boca Raton, FL, Nov. 2012, ISBN : 978-1-4398-7430-1.

Aslam, S., and 11 others, 2015. Net Flux Radiometer for a Saturn Probe. European Planetary Science Congress, 27th Sept. – 2nd Oct., 2015, Nantes, France.

Aslam, S., and 24 others, 2016. Dual-telescope multi-channel thermal-infrared radiometer for outer planet fly-by missions, Acta Astronautica, 128, 628-639.

Aslam, S., Achterberg, R. K., Cottini, V., Gorius, N., Hewagama, T., Irwin, P. G. J., Nixon, C. A., Simon, A. A., Quilligan, G., Villanueva, G., 2018. Net Flux Radiometer for the Ice Giants, 49th Lunar and Planetary Science Conference 2018, (LPI Contrib. No. 2083, 2675), The Woodlands, TX, USA.

Aslam, S., Achterberg, R. K., Calcutt, S. B., Cottini, V., Gorius, N., Hewagama, T., Irwin, P. G. J., Nixon, C. A., Simon, A. A., Quilligan, G., Villanueva, G., 2019. A compact, Versatile Net Flux Radiometer for Ice Giant Probes, Proceedings of the International Planetary Probe Workshop, Oxford, UK.

Atreya S. K., Wong, A-S., 2004. Clouds of Neptune and Uranus, Proceedings, International Planetary Probe Workshop, NASA Ames, CP-2004-213456.

Atreya, S. K., Wong, A.-S., 2005. Coupled Clouds and Chemistry of the Giant Planets – A Case for Multiprobes. *Space Science Reviews* **116**, 121-136.

Baines, K. H., Hammel, H. B., 1994. Clouds, hazes, and the stratospheric methane abundance in Neptune. Icarus 109, 20-39.

Baines, K. H., Mickelson, M. E., Larson, L. E., Ferguson, D. W., 1995. The abundances of methane and ortho/para hydrogen on Uranus and Neptune: Implications of New Laboratory 4-0 H_2 quadrupole line parameters. *Icarus* **114**, 328-340.

Bishop, J., Atreya S. K., Romani P. N., Orton G. S., Sandel B. R., Yelle, R. V., 1995. Book Chapter in Neptune and Triton by D. P. Cruikshank, Mildred Shapley Matthews, A. M. Schumann.

ISBN-10: 0816515255. ISBN-13:9780816515257. Pub. Date: 11/01/1995.Neptune and Triton, p. 4272,838 Cruikshank, D. P., ed., University of Arizona Press.

de Pater, I., Massie, S., 1985. Models of the millimeter-centimeter spectra of the giant planets, Icarus 62, 143-71

de Pater, I., Romani, P.N., Atreya, S.K., 1989. Uranus' deep atmosphere revealed. Icarus 82, 288–313.

de Pater, I., Romani, P.N., Atreya., S.K., 1991. Possible microwave absorption by H2S gas in Uranus' and Neptune's atmospheres. Icarus 91, 220–233.

de Pater I., Sromovsky, L. A., Fry P. M., Hammel, H., B., Baranec, C., Satanagi, K. M. 2015. Icarus, 252, 121.

Dodson-Robinson, S. E., Bodenheimer, P., 2010. The formation of Uranus and Neptune in solid-rich feeding zones: Connecting chemistry and dynamics. Icarus 207, 491-498.

Ice Giants Pre-Decadal Survey Mission Study Report., 2017. (JPLD-100520), https://www.lpi.usra.edu/icegiants/mission_study/

Irwin, P.G.J., Teanby, N.A., de Kok, R., Fletcher, L.N., Howett, C.J.A., Tsang, C.C.C., Wilson, C.F., Calcutt, S.B., Nixon, C.A. and P. D. Parrish., 2008. The NEMESIS planetary atmosphere radiative transfer and retrieval tool. *Journal of Quantitative Spectroscopy and Radiative Transfer*, 109:1136–1150. doi: 10.1016/j.jqsrt.2007.11.006.

Irwin, P. G. J., 2009. Giant Planets of Our Solar System. Giant Planets of Our Solar System: Atmospheres, Composition, and Structure, Springer Praxis Books. ISBN 978-3-540-85157-8. Springer Berlin Heidelberg, 2009.

Irwin, P. G. J., Wong, M. H., Simon, A. A., Orton, G. S., Toledo, D., 2017. HST/WFC3 observations of Uranus' 2014 storm clouds and comparison with VLT/SINFONI and IRTF/Spex observations. *Icarus* 288, 99-119.

Irwin, P.G.J., Toledo, D., Garland, R., Teanby, N.A., Fletcher, L.N., Orton, G.S., Bézard, B., 2018. Detection of hydrogen sulfide above the clouds in Uranus's atmosphere. Nature Astronomy 2, 420 – 427.

Irwin, P.G.J., Toledo, D., Garland, R., Teanby, N.A., Fletcher, L.N., Orton, G.S., Bézard, B., 2019. Probable detection of hydrogen sulphide (H_2S) in Neptune's atmosphere. Icarus 321, 550 – 563.

Karkoschka, E. and Tomasko, M.G., 2011. *Icarus, 211,* 780 – 797

Lissauer, J. J. 2005. Formation of the Outer Planets. Space Science Reviews 116, 11-24.

Mousis, O., and 55 others., 2018. Scientific rationale for Uranus and Neptune *in situ* explorations, Planetary and Space Science, 155, 12-40.

Pearl, J. C., Conrath, B. J., Hanel, R. A., Pirraglia, J. A., 1990. The albedo, effective temperature, and energy balance of Uranus, as determined from Voyager IRIS data. *Icarus* **84**, 12-28. planets. Icarus 62, 143–171.

Quilligan, G., Aslam, S., Lakew, B., DuMonthier, J., Katz, R., and Kleyner, I., 2014. A 0.18µm CMOS Thermopile Readout ASIC Immune to 50 Mrad Total Ionizing Dose (Si) and Single Event Latchup to 174 MeV-cm^2/mg. International Workshop on Instrumentation for Planetary Missions (IPM- 2014), November 2014, Greenbelt, MD 20771.

Quilligan, G., DuMonthier, J., Aslam, S., Lakew, B., Kleyner, I., Katz, R., 2015. Thermal Radiometer Signal Processing using Radiation Hard CMOS Application Specific Integrated Circuits for use in Harsh Planetary Environments. European Planetary Science Congress 2015, 27 Sept.-2 Oct., 2015 in Nantes, France.

Quilligan, G., Aslam, S., 2017. Auto-zero Differential Amplifier, US Patent 9,685,913 B2.

Quilligan, G., Aslam, S., 2018. Gated CDS Integrator, US Patent 10,158,335 B2.

Quilligan, G., Aslam, S., 2018. Gated CDS Integrator, US Patent 9,985,594 B2.

Sromovsky, L. A., Best, F. A., Revercomb, H. E., Hayden, J., 1992. Galileo Net Flux Radiometer Experiment. *Space Science Reviews* **60**, 233-262.

Sromovsky, L. A., Collard, A. D., Fry, P. M., Orton, G.S., Lemmon, M. T., Tomasko, M. G., Freedman, R. S., 1998. Galileo probe measurements of thermal and solar radiation fluxes in the Jovian atmosphere. *Journal of Geophysical Research* **103**, 22929-22977.

Tomasko, M. G., Buchhauser, D., Bushroe, M., Dafoe, L. E., Doose, L. R., Eible, A., Fellows, C., McFarlane, E., Prout, G. M., Pringle, M. J., Rizk, B., See, C., Smith, P. H., Tsetsenekos, K., . 2002. The Descent Imager/Spectral Radiometer (DISR) Experiment on the Huygens Entry Probe of Titan, Space Science Reviews*,* 104: 469-551.

Turrini, D., and 14 others, 2014. The comparative exploration of the ice giant planets with twin spacecraft: Unveiling the history of our Solar System, Planetary and Space Science 104, 93-107.

Villanueva, G. and 7 others, 2017. "Planetary Spectrum Generator (PSG): an online tool to synthesize spectra of Comets, Small Bodies and (exo)Planets"; "Asteroids, Comets, Meteors (ACM) conference", Montevideo, 2017. Planetary Spectrum Generator (https://psg.gsfc.nasa.gov).

Vision and Voyages for Planetary Science in the Decade 2013-2022, (NRC 2011), https://solarsystem.nasa.gov/2013decadal/